SPECIAL
Global Precipitation Measurement (GPM)
COLLECTION

The GPM-DPR Blind Zone Effect on Satellite-Based Radar Estimation of Precipitation over the Andes from a Ground-Based Ka-band Profiler Perspective

JAIRO M. VALDIVIA,[a] PATRICK N. GATLIN,[b] SHAILENDRA KUMAR,[a,c] DANNY SCIPIÓN,[a] YAMINA SILVA,[a,d] AND WALTER A. PETERSEN[b]

[a] *Instituto Geofísico del Perú, Lima, Peru*
[b] *NASA Marshall Space Flight Center, Huntsville, Alabama*
[c] *Department of Environmental Science, SRM University-AP, Neerukonda, Andhra Pradesh, India*
[d] *Instituto Nacional de Investigación en Glaciares y Ecosistemas de Montaña, Lima, Peru*

(Manuscript received 15 September 2020, in final form 10 January 2022)

ABSTRACT: A vertically pointing Ka-band radar (Metek MIRA-35C) installed at the Instituto Geofísico del Perú, Atmospheric Microphysics and Radiation Laboratory (LAMAR) Huancayo Observatory, which is located at an elevation of 3.3 km MSL in the Andes Mountains of Peru, is used to investigate the effects of terrain on satellite-based precipitation measurement in the Andes. We compare the vertical structure of precipitation observed by the MIRA-35C with Ka-band radar measurements from the Dual-Frequency Precipitation Radar (DPR) on board the Global Precipitation Measurement (GPM) mission core satellite using an approach based on Taylor's hypothesis of frozen turbulence that attempts to reduce the impact of spatiotemporal offsets between these two radar measurements. From 3 April 2014 to 20 May 2018, the DPR measured precipitation near LAMAR during 15 of its 157 coincident overpasses. There were six simultaneous observations with MIRA-35C. We found that the average of the DPR's lowest clutter-free bin is 1.62 km AGL, but the presence of precipitation worsens the situation, causing a 0.4-km-deeper algorithm-detected blind zone for the DPR at the Huancayo Observatory. In the study area, the depth of the clutter layer observed with DPR often extends above the melting layer but can be highly variable, extending even as high as 5 km AGL. These results suggest that DPR estimates of stratiform precipitation over the Andes Mountains are likely underestimated because of the terrain effects on the satellite measurements and problems in its blind zone detection algorithms, highlighting the difficulty in estimating precipitation in mountainous terrain from spaceborne radar.

KEYWORDS: Drop size distribution; Orographic effects; In situ atmospheric observations; Profilers, atmospheric; Radars/radar observations; Satellite observations

1. Introduction and motivation

Peru is a country vulnerable to natural hazards from hydrometeorological origin with great social and economic impact (Cardona et al. 2012; Welle and Birkmann 2015). The complex topography of the Andes, which covers much of the Peruvian territory, complicates satellite-based retrieval of precipitation (Derin et al. 2016; Mourre et al. 2016; Mantas et al. 2015; Scheel et al. 2011). Although regional numerical weather prediction models have been used to study orographic precipitation in different mountainous regions, including the Andes (Barrett et al. 2009; Viale and Norte 2009; Junquas et al. 2018), the models generally overestimate the precipitation (e.g., Moya-Álvarez et al. 2018a,b, 2019). The findings of Mourre et al. (2016) indicate neither Tropical Rainfall Measuring Mission products nor the Weather Research and Forecasting Model can meet the challenge of representing both accumulated quantities of precipitation and frequency of occurrence at the short time scales (subdaily and daily) required for glacio-hydrological studies over the Andes Mountains. The problem is compounded by the disagreement among different types of rainfall products and results of hydrological studies in this region and other complex terrain regions (Derin et al. 2019).

In mountainous regions, orographic effects on cloud microphysics often result in a heterogeneous distribution of the precipitation (Roe 2005). Furthermore, widely varying topography presents practical limitations for precipitation mapping by traditional observing networks (e.g., gauges, scanning weather radars). Being able to measure the full vertical structure of precipitation can facilitate a more accurate depiction of precipitation in mountainous regions (Houze 2012). Although the Global Precipitation Measurement (GPM) mission, with its Dual-Frequency Precipitation Radar (DPR), provides these measurements on a global scale (Hou et al. 2014; Skofronick-Jackson et al. 2018), its algorithms largely underestimate precipitation in complex terrain (e.g., Speirs et al. 2017; Cao et al. 2018). DPR retrievals in mountainous regions are severely complicated by the surface returns (i.e., clutter) that limit how close to the ground the precipitation estimate can be obtained, which can severely affect the precipitation estimate (e.g., Arulraj and Barros 2019b). The performance of GPM-DPR algorithms has been assessed in the central Peruvian Andes through in situ observations (Del Castillo-Velarde et al. 2021), where it was found that

Corresponding author: Jairo M. Valdivia, valdiviaprado.ing@gmail.com

DOI: 10.1175/JAMC-D-20-0211.1

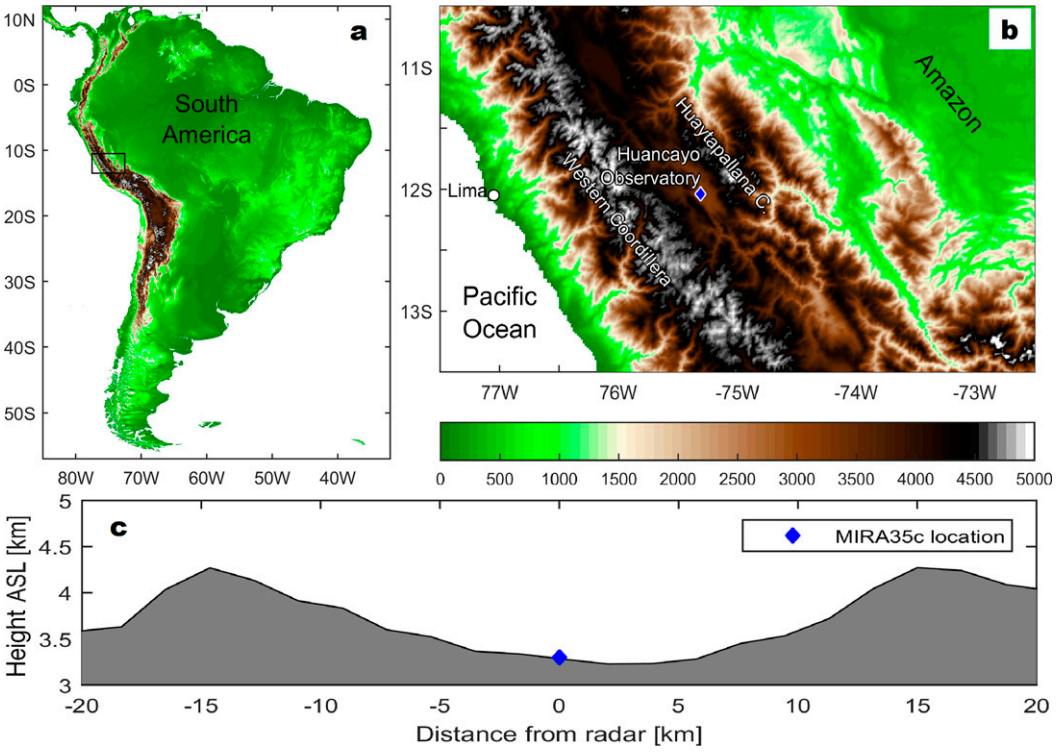

FIG. 1. Huancayo Observatory location and topography around this location. (a) Study area from South America perspective. (b) The area inside the black-outlined box in (a). The Huaytapallana cordillera is located to the east of the Huancayo Observatory. The color bar indicates the altitude in meters MSL. (c) The topography cross section at 12°S centered at the MIRA-35C location.

the high variability of convective precipitation and the very small mean diameters (1–1.6 mm) in the light rainfall rates (0.5–2.0 mm h^{-1}) were the main difficulties of the algorithms of the DPR. Chavez et al. (2020) have noted the difficulty DPR's Ku-band radar has detecting the shallow precipitation systems that frequently occur within the elevated Mantaro Valley of Peru during the monsoon (December to March). This is further complicated by the melting layer, which in elevated terrain is often relatively close to the ground such that the lowest clutter-free bin of the DPR is above the liquid layer resulting in a biased estimate of near surface precipitation (Speirs et al. 2017; Chavez et al. 2020). In operational radar-based precipitation estimation, the vertical profile of reflectivity (VPR) has been applied in such instances (e.g., Joss and Lee 1995; Germann et al. 2006; Wen et al. 2016). However, such approaches largely assume the VPR is constant below the melting layer, whereas we know this can be false (e.g., Cao et al. 2013; Gatlin et al. 2018). To improve satellite-based precipitation retrieval, especially over complex topography like the Peruvian Andes, it is critical that we understand how precipitation varies within this DPR blind zone (i.e., below its lowest clutter-free bin).

In this study we focus on the DPR's representation of near surface precipitation in the Peruvian Andes and how it is affected by the blind zone. We use the MIRA-35C Ka-band radar to investigate the vertical variability of precipitation and compare with DPR Ka-band measurements, primarily within the DPR blind zone. We also employ an approach to mitigate the influence of sampling volume differences when comparing measurements from the two instruments.

The study area, instruments descriptions, and case studies are described in section 2. Section 3 presents the results of simultaneous observations and the effect of the blind zone in the DPR retrieval over our study area. The implications of these results to the GPM mission are outlined in section 4, followed by conclusions in section 5. This work aims to give a general insight of possible sources of uncertainty in DPR retrievals of precipitation over the complex topography of the Andes.

2. Instrument description and data

a. Study area

Our study area focuses on the Huancayo Observatory at the Instituto Geofísco del Perú Atmospheric Microphysics and Radiation Laboratory (LAMAR; 12.0°S, 75.3°W, 3313 m MSL) in Mantaro Valley, which is nestled in the Andes between the Cordillera Occidental and Huaytapallana Cordillera in central Peru (Fig. 1). Annual rainfall at this location is 700 mm, and it is characterized as being dry in winter (austral) and rainy in summer (with maximum precipitation in February). According to Köppen–Geiger classification (Peel et al. 2007), Mantaro Valley has a temperate highland climate

TABLE 1. MIRA-35C specifications.

Frequency	34.85 GHz
Peak power	2.5 kW
Receiver	Single polarization
Operation mode	Pulsed
Beamwidth	0.6°
Antenna type	Cassegrain
Range resolution	31 m
Temporal resolution	5.6 s
No. of range gates	415
No. of spectral bins	128

(Cwb). A detailed description of LAMAR can be found in Flores-Rojas et al. (2021a).

b. *MIRA-35C processing*

The MIRA-35C, manufactured by Meteorologische Messtechnik GmbH (METEK), is a vertically pointing, pulsed Doppler radar operating at 34.85 GHz (λ = 8.6 mm; Ka band). It was installed on 26 December 2015 in LAMAR–Huancayo Observatory. The manufacturer stated that the radar calibration was performed on metal spheres just before the installation of the radar at the Huancayo Observatory. It uses a magnetron to transmit a linear polarized pulse. The radar simultaneously receives both co- and cross-polarized signals to measure the Doppler spectra with a Nyquist velocity of ± 10.3 m s^{-1}. The system has a vertical range resolution of 31 m from 150 m and 13 km above ground, but range bins below 250 m are not used because of near-field clutter. The complete specifications of this MIRA-35C installed at LAMAR are given in Table 1.

The retrieval of drop size distribution (DSD) and integral rain parameters from vertically pointing Doppler radar measurements is well documented (e.g., Atlas et al. 1973; Peters et al. 2002, 2005, 2010; Maahn and Kollias 2012; Das and Maitra 2016; Valdivia et al. 2020b), and here we only summarize the relevant steps used for this study. The observed noise spectra are removed by the MIRA-35C signal-processing software, which utilizes a noise-estimation module based on the method by Hildebrand and Sekhon (1974).

The Doppler spectra is related to the DSD by

$$N(D,z) = \frac{\eta(D,z)}{\sigma(D)}, \tag{1}$$

where $N(D, z)$ is the DSD at a height z and $\eta(D, z)$ is the spectral volume backscattering cross section (i.e., spectral reflectivity). The single-particle backscattering cross section $\sigma(D)$ of a sphere with diameter D is calculated using Mie-scattering theory. Assuming no vertical wind, the terminal fall velocity v of falling raindrops can be related to their diameter via the Atlas et al. (1973) fit to the Gunn and Kinzer (1949) raindrop v measurements,

$$D(v,z) = \frac{1}{0.6}\ln\left[\frac{10.3}{9.65 - \dfrac{v}{\delta(z)}}\right], \tag{2}$$

where $\delta(z)$ is an adjustment that accounts for the height dependence of air density on the v of raindrops (Foote and Du Toit 1969). We fit a second-order polynomial to the air density correction factors used by Atlas et al. (1973) to obtain this adjustment of as a function of altitude,

$$\delta(z) = (1 + 3.68 \times 10^{-5} z + 1.71 \times 10^{-9} z^2). \tag{3}$$

Combining (2) with (1), the spectral reflectivity can be expressed in terms of Doppler velocity as

$$\eta(D,z) = \eta(v,z)\frac{\partial v}{\partial D(v,z)}, \tag{4}$$

where $\eta(v, z)$ is the Doppler velocity spectrum at each height.

The MIRA-35C signal can be significantly attenuated within rain. Hence, we account for this prior to deriving any integral rain parameters. The rain attenuation coefficient κ_r (m^{-1}) is computed using the Mie-scattering theory from drop size distribution by

$$\kappa_r = \int \sigma_e(D) N(D)\, dD, \tag{5}$$

where σ_e is the single-particle extinction cross section. The rain attenuation coefficient is related to the two way attenuation A in the following range gate by

$$A(z_2) = \exp[-2\kappa_r(z_1)\Delta z]. \tag{6}$$

The radar reflectivity factor (mm^6 m^{-3}) is defined as

$$Z = \int N(D) D^6\, dD. \tag{7}$$

The equivalent radar reflectivity factor is given by

$$Z_e = \frac{\int \eta(v)\, dv}{\left(\dfrac{\pi^5}{\lambda^4}\right)|K^2|}, \tag{8}$$

with the dielectric constant $|K^2| \approx 0.92$ corresponding to liquid water. The Z_e is identical to that given by (7) within the region of Rayleigh scattering (i.e., $D \ll \lambda$).

The mass-weighted mean diameter (mm),

$$D_m = \frac{\int N(D) D^4\, dD}{\int N(D) D^3\, dD}, \tag{9}$$

and the normalized number concentration N_w (mm^{-1} m^{-3}),

$$N_w = \frac{4^4}{\pi \rho_w}\frac{10^3 q}{D_m^4}, \tag{10}$$

describe the DSD. In (10), q (g m^{-3}) is the liquid water content defined as

$$q = (1 \times 10^{-3})\rho_w(\pi/6)\int N(D) D^3\, dD, \tag{11}$$

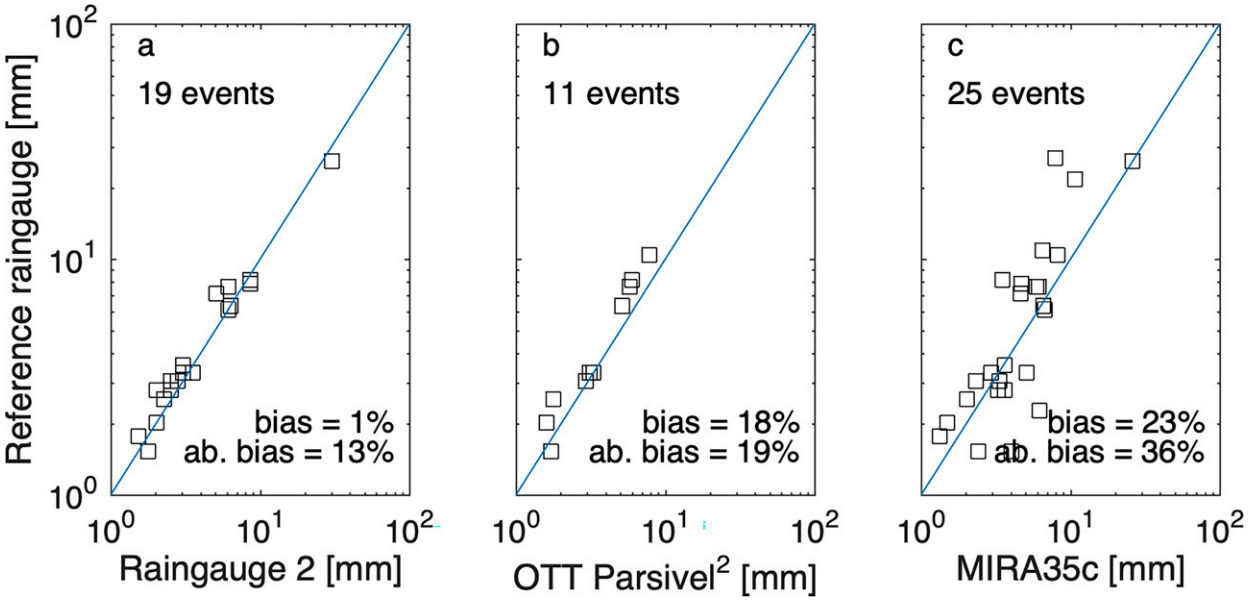

FIG. 2. Comparison of rain events totals (a) between the reference rain gauge and rain gauge 2, (b) between the reference rain gauge and OTT Parsivel^2, and (c) between the reference rain gauge and MIRA-35C.

and the density of water $\rho_w = 1$ g cm^{-3}. From the DSD and v (m s^{-1}), we compute the rainfall rate R (mm h^{-1}) as

$$R = (6 \times 10^{-4} \times \pi) \int N(D) v(D) D^3 \, dD. \tag{12}$$

Note that this DSD derivation is based on falling raindrops and is valid for liquid precipitation only. No adjustments are made for MIRA-35C retrievals within regions of mixed-phase or solid precipitation since the focus of this study is on the region below the melting layer.

To assess the performance of the MIRA-35C, we compared the rainfall rates retrieved from the lowest height range bin (250 m) of the MIRA-35C with the rainfall measured by collocated tipping-bucket rain gauges and an OTT HydroMet GmbH Parsivel^2 optical disdrometer (Fig. 2). The events shown in Fig. 2 occurred in the period January–April 2018, when all instruments were operational. MIRA-35C underestimates the precipitation with a bias of 23% and absolute bias of 36%. The OTT Parsivel^2 underestimates the precipitation as well with a bias of 18% and the absolute bias of 19%. Parsivel^2 description, rain gauge instrumentation, characteristics, and datasets can be found in Valdivia et al. (2020a).

c. GPM-2ADPR data

The satellite-based precipitation observations we use were obtained with the GPM DPR, which operates at both Ku- and Ka-band radar frequencies and has a footprint of approximately 5 km in diameter at nadir (Hou et al. 2014). For this study we use data from DPR's Ka-band high sensitivity (HS) scans, which have a swath width of 120 km and vertical resolution of 500 m, the Ku-band normal sensitivity (NS) scans, which have a swath width of 245 km and vertical resolution of 250 m. The bins are matched to the inner swath of Ku-NS providing a matched scan (MS) swath of 120 km. Both radar echoes are oversampled at twice the rate of corresponding resolutions: 125 m for matched beams and 250 m for Ka-HS. This dataset is contained within the GPM 2ADPR, version 06, product (Iguchi and Meneghini 2017; Iguchi et al. 2018) available from NASA's Precipitation Processing System (http://pps.gsfc.nasa.gov). We use the 2ADPR product for this study in the period from 3 April 2014 to 20 May 2018. On 21 May 2018, the DPR's Ka-band's HS scan was changed from the inner to outer swath of the Ku-band radar (Furukawa et al. 2018).

From the Ka-band HS scans in the 2ADPR product, we use the measured radar reflectivity factor with no attenuation correction (zFactorMeasured), the radar reflectivity factor with attenuation correction (zFactorCorrected), rain rate R, mass-weighted mean diameter D_m, and the normalized number concentration N_w for comparison with that obtained from the MIRA-35C measurements.

d. Spatiotemporal averaging technique

Since the sampling volume of the MIRA-35C is significantly smaller than that of the DPR, we average the MIRA-35C observations to reduce some of the uncertainty that may arise as a result. The objective is to find a suitable temporal window that represents the spatial distribution of each event. We use horizontal wind velocity to assess this. The wind velocity was measured by the boundary layer and troposphere radar (BLTR), which operates at a frequency of 50 MHz and is primarily sensitive only to Bragg scatter (i.e., clear-air returns) except during times of intense precipitation (Ralph 1995; Rao et al. 1999). If we assume the ambient atmospheric flow is purely laminar (i.e., vertical motion is negligible), we can apply Taylor's hypothesis of frozen turbulence (Taylor 1938).

Both Zawadzki (1973) and Lee et al. (2007) demonstrate the validity of Taylor's hypothesis for DSD moments and their intrarelationships. The effective separation distance δ_E of precipitation within the DPR footprint diameter (5 km) using Taylor's hypothesis is defined as follows:

$$\Delta t = t_j - t_i, \tag{13}$$

$$\Delta x = x_j - x_i - u\Delta t, \tag{14}$$

$$\Delta y = y_j - y_i - v\Delta t, \text{ and} \tag{15}$$

$$\delta_E = \sqrt{\Delta x^2 + \Delta y^2}, \tag{16}$$

where x and y are the zonal and meridional separation distances between i and j measurements, respectively; u and v are zonal and meridional wind from BLTR, respectively; and Δt is the time between measurements. Since the MIRA-35C observations are taken vertically, we can treat this as a one-dimensional Eulerian problem using the wind velocity v, and combine (14)–(16) to obtain the following temporal averaging window centered on the DPR overpass time,

$$\Delta t = \delta_E / v. \tag{17}$$

Hence, given the BLTR measurements of v and spatial separation of the DPR and MIRA-35C observations we obtain Δt, which represents the spatiotemporal variation of the precipitation during the overpass time. To assess the sensitivity of the VPR as a function of time, Δt was arbitrarily multiplied by 2, and it is included in the analysis.

3. Results

During the period from 3 April 2014 to 20 May 2018, 157 DPR overpasses occurred within 5-km of LAMAR and 15 of these contained precipitation. Six of those precipitation events were also observed with the MIRA-35C (Fig. 3). An overview of these six events is given in the Table 2.

Applying (17) to the column-average horizontal wind velocities measured by the BLTR during the DPR overpass results in averaging times of 28.6, 9.7, 11.9, 17.6, 15.6, and 14.1 min for 23 February 2016 (stratiform), 6 January 2017 (convective), 13 February 2017 (stratiform), August 15 (convective), 9 April 2016 (stratiform), and 8 October 2017 (convective), events, respectively. We compare the MIRA-35C observations during these time windows centered at the overpass time with the DPR for each event. The DPR's bias is defined here as bias = $Y - X$, where X is the reference MIRA-35C measurement.

a. Comparison of vertical profiles of precipitation

In this section, we compare vertical profiles from 2ADPR (Ka-band HS scans) with the time-averaged MIRA-35C (Ka band) observations centered on the DPR overpass for each precipitation event (Fig. 4). We included in the analysis all the DPR-HS profiles that were within 5 km of the location of the MIRA-35C. Seventeen DPR-HS profiles were found in the six events. Three of these events were identified as stratiform and three as convective.

1) STRATIFORM EVENTS

Three stratiform events were found, corresponding to the dates of 23–24 February 2016, 13 February 2017, and 9 April 2017 (herein E1, E3, and E5; Figs. 3a,c,e). The overpass times for these events were 0140, 0636, and 0150 UTC. The bright band was evident in the MIRA-35C VPRs corresponding to the altitudes of 5.3, 4.5, and 4.6 km MSL (Figs. 4a–e,k–o,u–y). These DPR-HS profiles for these stratiform events are from slightly off-nadir rays (6.4° and 7.2°). The lowest clutter-free bin (i.e., binClutterFreeBottom in 2ADPR) was above the bright band in all cases except for event E1 in which one of the three DPR profiles is at the same height as the bright band and another is 0.5 km below the bright band (Fig. 4a).

In the E1 event, a bright band in MIRA-35C VPR with a maximum reflectivity of 21 dBZ is observed around 5.2 km MSL at the overpass time (Figs. 4a–e). In the DPR reflectivity profiles, there is little evidence of a bright band, and its measured reflectivity matches quite well with MIRA-35C Z_e within and just below the melting layer. The VPR measured by the DPR above its lowest clutter-free bin is greater than that measured by the MIRA-35C and exhibits an overall weaker decrease in reflectivity aloft when compared with that of the MIRA-35C VPR (Fig. 4a). The 2ADPR-corrected reflectivity profile is very similar to that of the MIRA-35C, especially for the longer averaging window (Fig. 4b). The 2ADPR extrapolates its retrieval from the lowest clutter-free bin to the surface (i.e., assumes a constant profile). Both the DPR and MIRA-35C retrieve a rainfall rate R around 0.2–0.4 mm h^{-1} below the ML with the shorter averaging window of the MIRA-35C exhibiting slightly better agreement with the DPR retrievals of R. Below the ML, the MIRA-35C D_m is around 0.7 mm while all DPR profiles for this event estimate a D_m of 1.2 mm (Fig. 4d). Meanwhile, the DPR N_w profiles are underestimated and constant below the ML (Fig. 4e), whereas the N_w profile from MIRA-35C exhibits a decrease from around 4 log(mm^{-1} m^{-3}) below the ML to 3.8 log(mm^{-1} m^{-3}) near the ground. Caution must be used in drawing any conclusions from the comparisons within and above the melting layer since nonliquid particles were not accounted for in the MIRA-35C retrievals.

In the E3 event, a bright band is evident throughout the duration (8 h) at 4.5 km MSL (Fig. 3c). Four DPR profiles were found, consisting of ray angles at 7.2° and 6.4° relative to nadir. In all cases, the DPR's lowest clutter-free bin is around 5.5 km MSL, which is about 1 km higher than MIRA-35C's bright band (Fig. 4k). The bright band in MIRA-35C VPR with maximum reflectivity of 21 dBZ is observed around 4.5 km MSL at the overpass time. The MIRA-35C peak reflectivity is found in both its measured Ze and the attenuation-corrected Z and exhibits little variability below the bright band. The reflectivity measured by DPR exhibits a much larger increase toward the ground than that measured by the MIRA-35C (Fig. 4k). However, much of this occurs within the DPR clutter region causing 2ADPR to extrapolate its

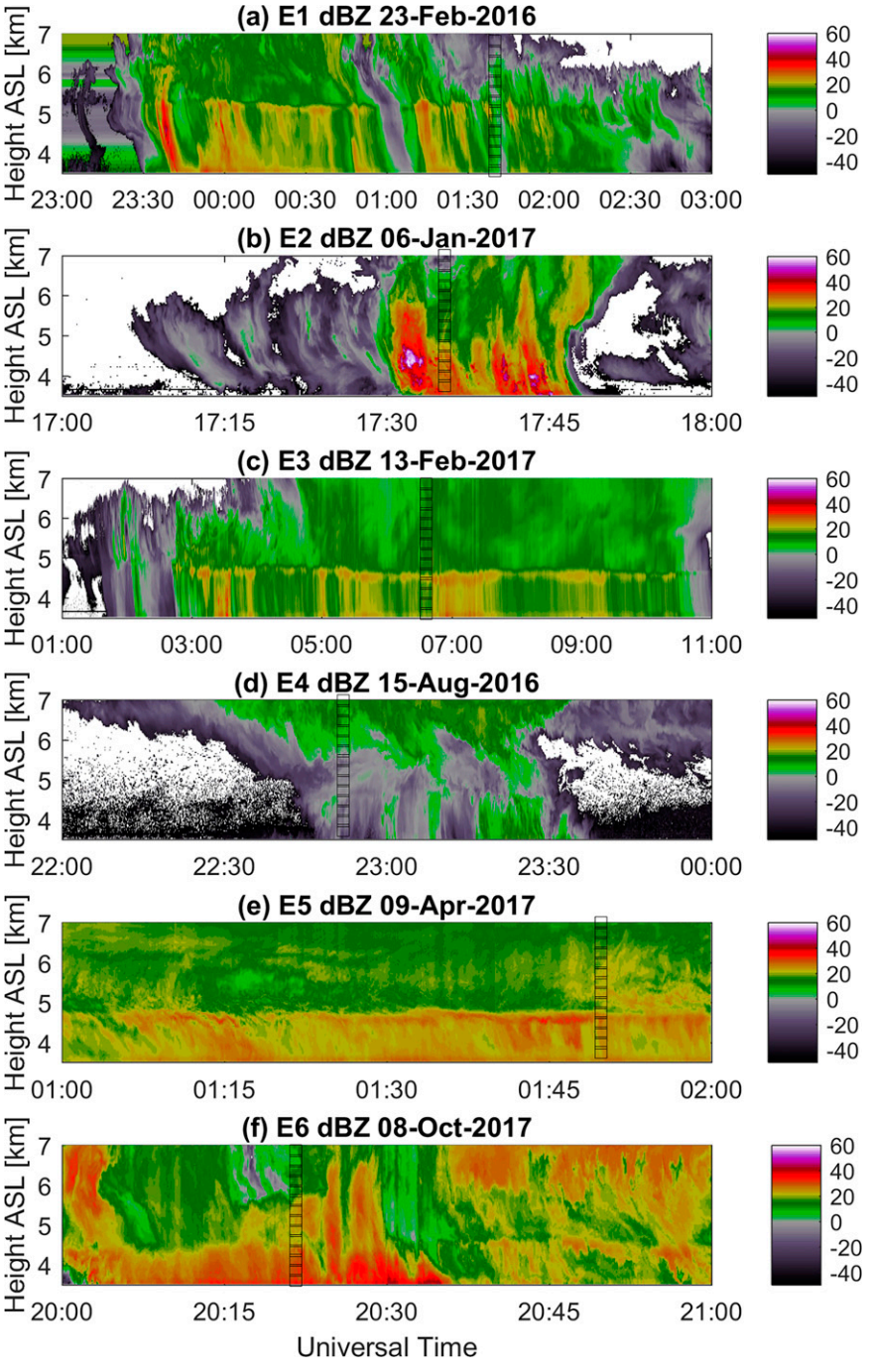

FIG. 3. Case studies of the reflectivity factor observed by MIRA-35C. The vertical open squares indicate the time of GPM overpass. (a) A stratiform event with embedded convection (23 Feb 2016). (b) A convective event (6 Jan 2017). (c) A stratiform event (13 Feb 2017). (d) A convective event (15 Aug 2016). (e) A stratiform event (9 Apr 2017). (f) An intense convective event (8 Oct 2017).

corrected reflectivity profile from its lowest clutter-free bin toward the surface where it closely matches that of the MIRA-35C (Fig. 4l). The DPR's estimated rain-rate profile is lower than MIRA-35C by 0.3–0.6 mm h^{-1} (Fig. 4m). The DSD profiles from 2ADPR are also constant below its lowest clutter-free bin, with D_m estimates 0.5 mm greater than the MIRA-35C and N_w an order of magnitude lower than retrieved in the rain layer from MIRA-35C.

TABLE 2. Main characteristic of the precipitation case studies.

Event	Overpass time (UTC)	Type	Duration	Mean horizontal wind velocity	Avg time
E1, 23–24 Feb 2016	0140:00[a]	Stratiform (embedded convection)	3 h	2.9 m s^{-1}	28.6 min
E2, 6 Jan 2017	1735:22	Convective	20 min	8.6 m s^{-1}	9.7 min
E3, 13 Feb 2017	0636:36	Stratiform	8 h	7.0 m s^{-1}	11.9 min
E4, 15 Aug 2016	2251:55	Convective	45 min	4.7 m s^{-1}	17.6 min
E5, 9 Apr 2017	0149:50	Stratiform	4 h	5.3 m s^{-1}	8.6 min
E6, 8 Oct 2017	2021:37	Convective	1.5 h	5.9 m s^{-1}	14.1 min

[a] This was an overnight event in which the overpass occurred on 24 February.

In the E5 event, a bright band in MIRA-35C VPR with a maximum reflectivity of 28 dBZ is observed around 4.6 km MSL at the overpass time (Figs. 4u,v). The MIRA-35C reflectivity exhibits a small decrease below the bright band toward the surface. Two DPR profiles were found from adjacent scans within 5-km of the MIRA-35C (both at a ray angle of 7.1°). The DPR's lowest clutter-free bin is around 5.5 km MSL, which is about 0.9 km higher than MIRA-35C's bright band. The 2ADPR profile with the lower clutter-free bin exhibits much better agreement with MIRA-35C than the other 2ADPR profile (Fig. 4v), but the overpass occurred during a time of a decreasing melting layer and enhanced brightband variability (Fig. 3e). The DPR's rain rate is 0.5–0.9 mm h^{-1} lower than the MIRA-35C (Fig. 4m). The 2ADPR DSD retrievals are in closer agreement for this event. The 2ADPR estimates of D_m below the ML are within 0.3 mm of MIRA-35C and N_w below the ML are around 3.0 log(mm^{-1} m^{-3}), 0.5 log(mm^{-1} m^{-3}) lower than MIRA-35C.

There is little difference in the MIRA-35C Δt and $\Delta t/2$ profiles for the E3 and E5 stratiform events. These profiles exhibited slightly larger differences in the E1 event. However, the overpass occurred during a period when some weak convection is seen above the ML (Fig. 3a).

2) CONVECTIVE EVENTS

Three convective events were found, corresponding to the dates of 6 January 2017, 15 August 2016, and 8 October 2017 (herein E2, E4, and E6; Figs. 3b,d,f). The GPM overpass times for these events were 1735, 2252, and 2021 UTC, respectively. There is no bright band evident in the MIRA-35C VPRs and there is considerable variability in the VPRs (Figs. 4f–j,p–t,z–dd). The DPR-HS scan angles for these convective events occurred between 1.1° and 7.2°. The three events are characterized by having high reflectivity values near the surface, except for the E4 event, which originated with convection in the area, but the convective core did not reach the Huancayo Observatory. An event in the area similar to E4 that occurred on 1 July 2016, was studied through modeling in Martínez-Castro et al. (2019). The convective events in the Mantaro Valley originate with the confluence of eastern moisture flows from the South American low-level jet and western Pacific Ocean moisture flows. The dynamics of intense events in the Mantaro Valley has been studied by Flores-Rojas et al. (2021b). Note that convective events occur in the afternoon between 1200 and 1800 LT (1700 and 2300 UTC), whereas stratiform events occur at night and early in the day (Table 2).

The variability of precipitation during the E2 event is evident in the reflectivity measured by the MIRA-35C (Fig. 3b). There is no ML evident in the VPR since the vertical motion is significantly affecting the MIRA-35C retrievals, which is apparent in the unrealistic variability exhibited in the DSD profiles during the time of the DPR overpass (Fig. 5b). Note that MIRA-35C's DSD retrieval assumes zero vertical wind velocity. Three DPR profiles were found at the scanning angles of 6.4° and 7.2° (Figs. 4f–j). The lowest clutter-free bins of the DPR are flagged at 5.5, 5.4, and 4.9 km MSL. The MIRA-35C measured Z profile increases below 7 km MSL, reaching a peak value of 33 dBZ around 4.2 km MSL, and then decreases 3 dB toward the ground (Fig. 4f). The Z_e measured by the DPR is similar at 4.2 km MSL but exhibits nearly a 6 dBZ increase toward the ground. Furthermore, the DPR exhibits a weaker decrease in reflectivity aloft than the MIRA-35C. The DPR's corrected reflectivity removes the low-level reflectivity enhancement and more closely resembles the Z_e from the MIRA-35C, but the vertical motion impacts on the MIRA-35C Z and other retrievals is evident (Figs. 4g–j). Near the ground, the DPR and MIRA-35C retrievals of R, D_m, and N_w are very similar. For this event, the averaging time of Δt helps to reduce the artificial variability caused by turbulence (Fig. 4g), but in the Ze profile is very similar to $\Delta t/2$ (Fig. 4f). The shorter averaging time exhibits the higher reflectivity, whereas it is not the case for other events.

In event E4, the reflectivity peak measured by the MIRA-35C of 13 dBZ is found in the highest part of the profile, near 7 km MSL, it decreases to −5.5 dBZ at 4.8 km MSL, then increases 3 dBZ at 0.5 km below, and near the surface it decreases to values between −5 and −9 dBZ (Fig. 4p). The DSD obtained for this event shows a constant increase in D_m toward the surface and an inverse behavior of N_w (Figs. 4s,t). It is likely that this behavior in the VPR is dominated by evaporation processes, shown as a loss in the concentration of small droplets (Fig. 5d) and loss of reflectivity near the surface (Fig. 3d). Two DPR profiles were found at the scanning angle of 4.1° (Figs. 4p–t). The lowest clutter-free bins of the DPR are flagged at 4.9 and 5.7 km MSL. Above this height, the measured reflectivity of the DPR is between 10 and 15 dBZ higher than that measured by the MIRA-35C. In the corrected reflectivity of the DPR, one of the profiles has a constant value of 21 dBZ, while the other has been marked as

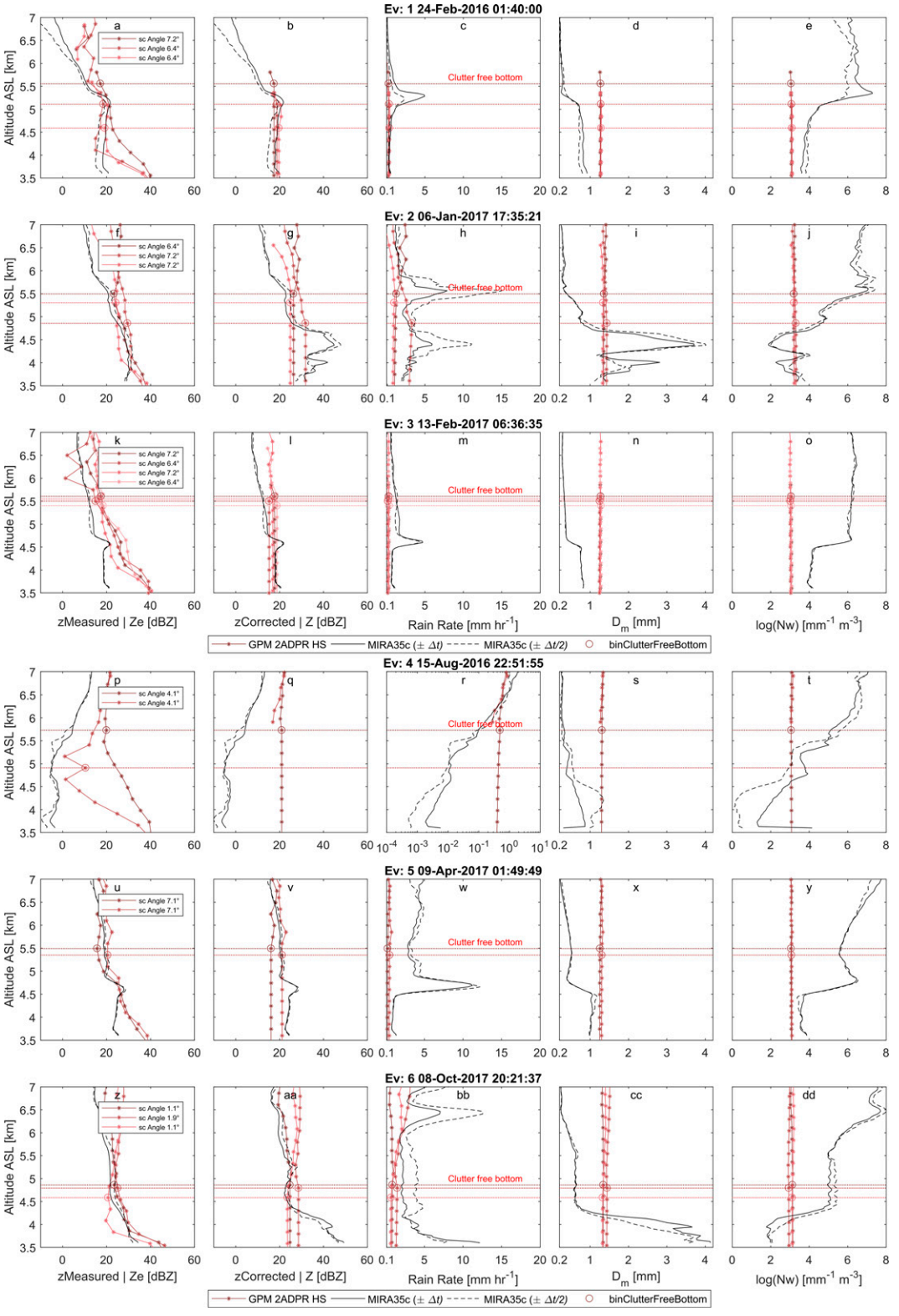

FIG. 4. Vertical profile of rainfall for the case studies, showing (a),(f),(k),(p),(u),(z) 2ADPR-HS zMeasured and MIRA-35C Z (dBZ); (b),(g),(l),(q),(v),(aa) 2ADPR-HS zCorrected and attenuation-corrected MIRA-35C Z (dBZ); (c),(h),(m),(r),(w),(bb) rain rate (mm h^{-1}); (d),(i),(n),(s),(x),(cc) mass-weighted mean diameter D_m (mm); and (e),(j),(o),(t),(y),(dd) normalized number concentration N_w [log(mm^{-1} m^{-3})]. Note that DSD retrieval is valid only for raindrops, so ice-layer retrievals, and above, are not to be trusted.

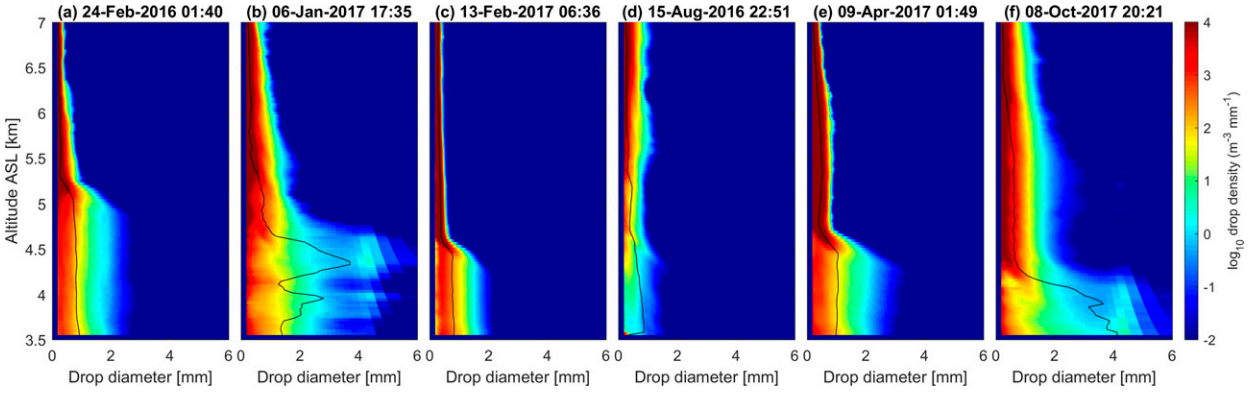

FIG. 5. Mean drop size distributions in the averaging period $\pm\Delta t$ retrieved by MIRA-35C for the six case studies; the black line indicates mean mass drop diameter D_m. Note that DSD retrieval is valid only for raindrops, so ice-layer retrievals, and above, are not to be trusted.

"missing values" from 5.9 km MSL to the surface (Fig. 4q). Because of the clutter, the DPR could not capture the variability of the profile near the surface, showing values of R, D_m, and N_w higher than those of MIRA-35C (Figs. 4r–t). The shorter averaging time ($\Delta t/2$) exhibits greater variability in the VPRs, in turn, lower reflectivity values.

In the E6 event, great variability can be observed in the VPR, which can be observed in the reflectivity measured by MIRA-35C (Fig. 3f). It can be seen that the Z_e peak of 34 dBZ is close to the surface (Fig. 4z). Vertical motion is significantly affecting MIRA-35C retrievals, which is evident in the unrealistic variability exhibited in the DSD profiles during the time of the DPR overpass (Fig. 5f). A "spurious mode" is observed in the concentration of the drops near the surface. This phenomenon results from the drops dragged by the wind vertical motion in the first fall of the backscattering cross

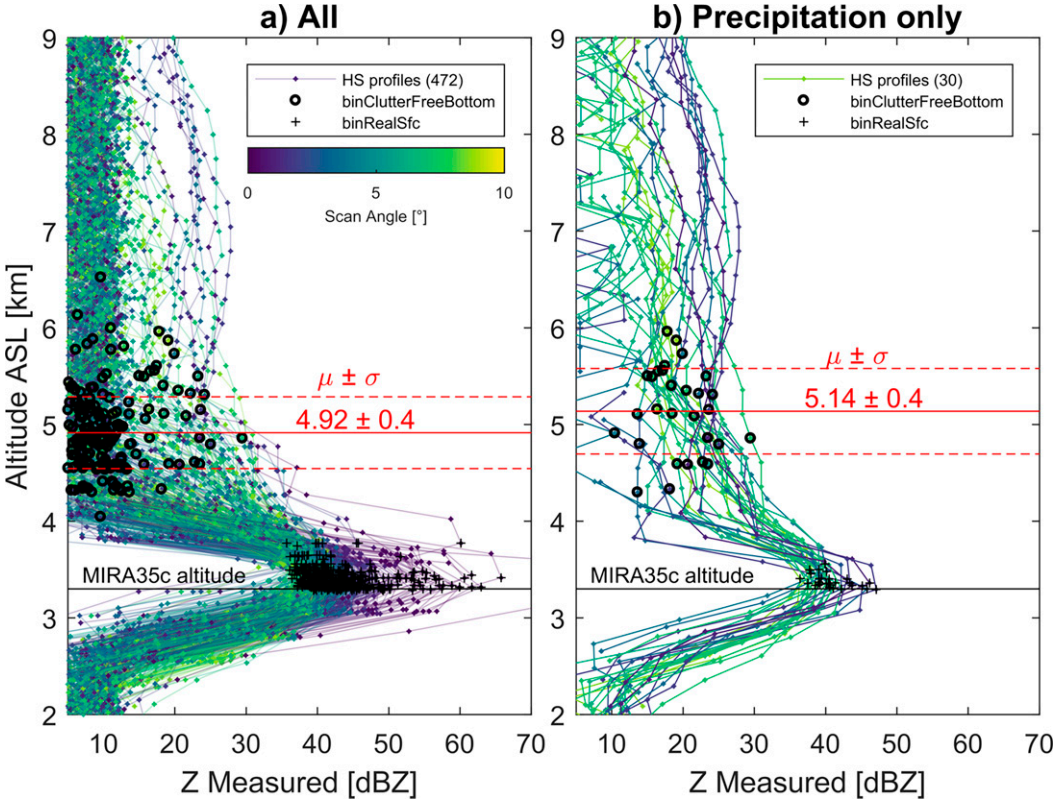

FIG. 6. (a) All dBZ measured profiles from the 2ADPR-HS over Huancayo Observatory, and (b) as in (a), but only for the profiles flagged as rain. The red solid and dashed lines indicate mean μ ± standard deviation σ of binClutterFreeBottom.

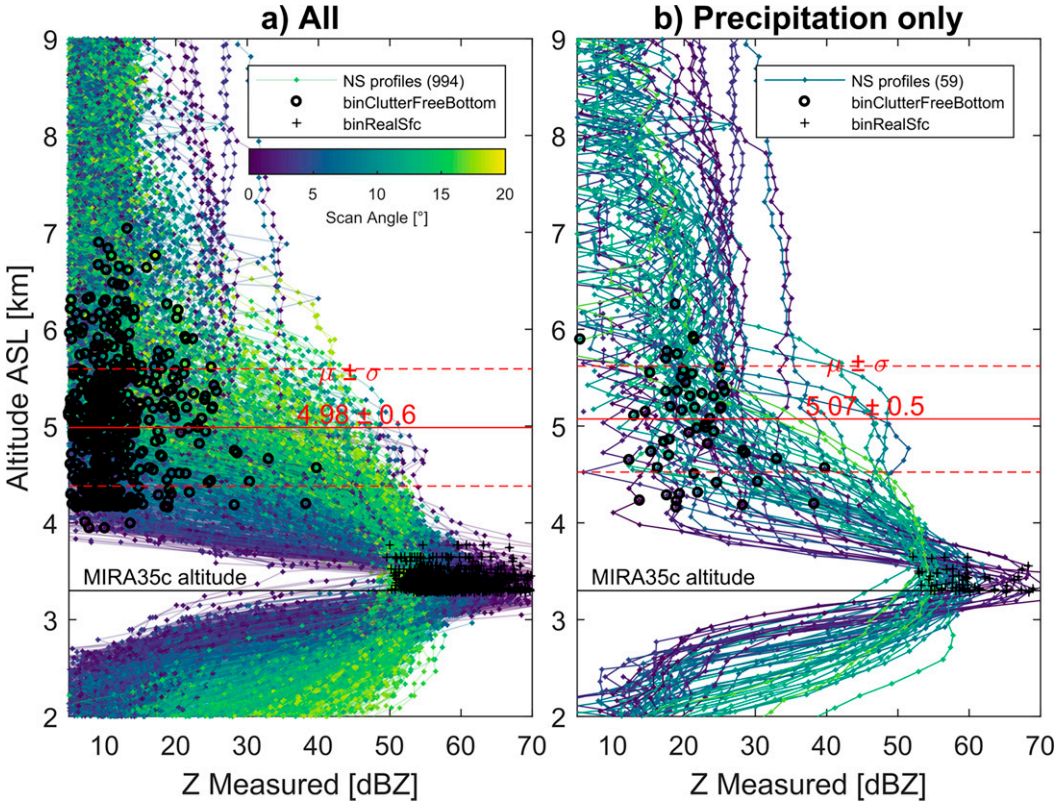

FIG. 7. As in Fig. 6, but for 2ADPR-NS.

section of the Mie-scattering theory (Mie notch) at 35 GHz (Valdivia et al. 2020b). The DSD artifact obtained also causes the corrected Z of MIRA-35C to increase by 13 dBZ near the surface, and consequently, it is to be expected that R and D_m are overestimated, while N_w is underestimated. Three DPR profiles were found at the scanning angles of 1.1° and 1.8° (Figs. 4z–dd), the lowest among all events. The clutter-free bottom bins of the DPR are flagged at 4.6, 4.8, and 4.9 km MSL. The VPR measured by the DPR above its lowest clutter-free bin is greater than that measured by the MIRA-35C and exhibits an overall weaker decrease in reflectivity aloft when compared with that of the MIRA-35C VPR (Fig. 4z). The DPR Z_e is very similar to that measured by the MIRA-35C, with differences less than 3 dBZ and Z also matches very well within 5.5 and 4.5 km MSL (Fig. 4aa). However, the corrected Z in DPR, the increase in reflectivity near the surface has been lost, which has created differences in the profiles of R, D_m, and N_w. For this event, the shorter averaging time ($\Delta t/2$) exhibits less variability in the VPRs, probably not significant.

b. Analysis of the precipitation within blind zone

The so-called blind zone in the DPR retrievals is defined as the zone between the surface and the range bin closest to the surface without clutter contamination [i.e., binClutterFreeBottom in the 2ADPR product (Iguchi et al. 2018)]. In these six precipitation events, the DPR blind zone extends 1.3–2.3 km above the ground. For the three stratiform events included in this study, the lowest clutter-free bin is within or above the MIRA-35C-inferred melting layer (ML) except for one profile from 24 February 2016 (Fig. 4a).

To evaluate the DPR's blind zone and the effects of ground clutter, we examined all of the DPR overpasses in our study period regardless of precipitation being present. Figure 6a shows all of the profiles collected by DPR-HS over the MIRA-35C location within 5 km, and Figs. 7a and 8a show all of the profiles collected by DPR-NS and DPR-MS, respectively.

The Z measured by DPR-HS exhibits a Gaussian-like distribution centered at ground level and extends 1.2 km above ground level. A similar behavior is observed in the DPR-MS (Fig. 8a). The DPR-NS profiles also exhibit a similar distribution peaked at the surface, but also exhibit more variability in the clutter region, which seems to be largely a result of the greater number off-nadir rays present in that scan (Fig. 7a). The lowest clutter-free bin identified in 2ADPR-HS is marked as black circles and the mean ± standard deviation is shown in solid and dashed red lines. The mean lowest clutter-free bin found for all HS overpasses occurs at 4.92 km MSL with a standard deviation of 0.4 km (Fig. 6a). In Fig. 6b we separate the profiles where precipitation was observed in the DPR-HS profiles. In the presence of precipitation, DPR-HS's mean lowest clutter-free bin is 0.22 km higher than when no precipitation is detected. In the DPR-NS overpasses, the mean lowest clutter-free bin occurs at 4.98 km MSL with a

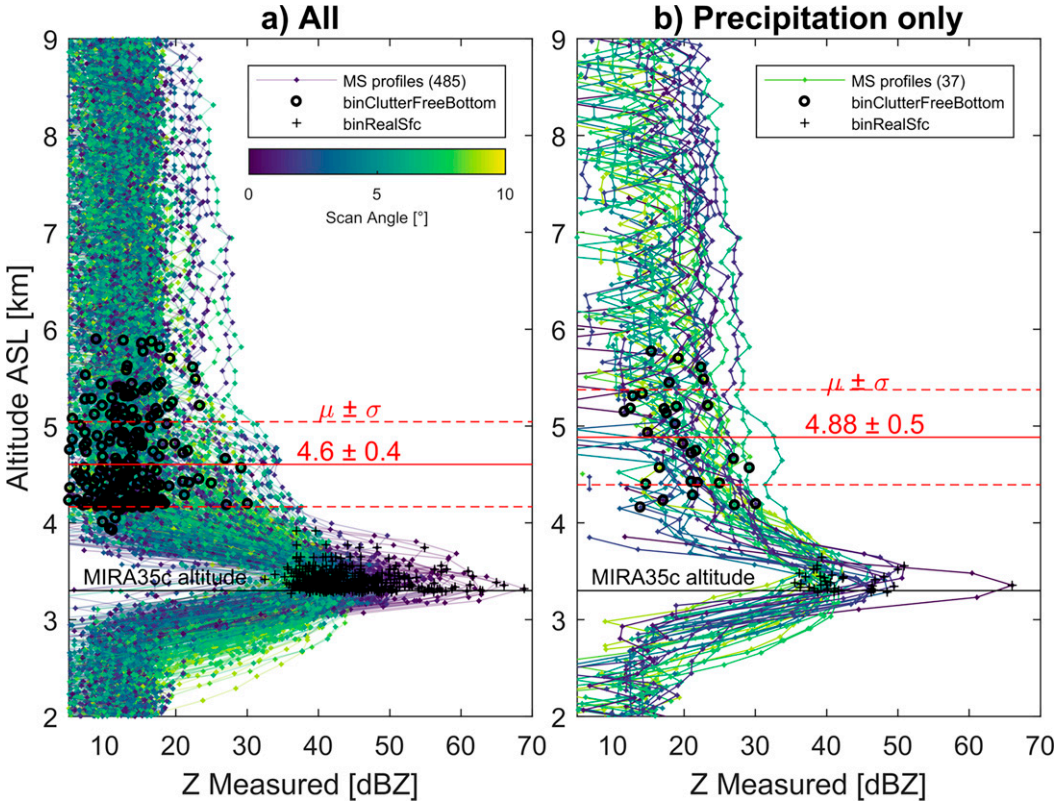

FIG. 8. As in Fig. 6, but for 2ADPR-MS.

standard deviation of 0.6 km (Fig. 7a). In DPR-MS overpasses (Fig. 8a), the mean lowest clutter-free bin occurs at 4.60 km MSL, about 0.35 km lower than in HS and NS, with a standard deviation of 0.4 km. In the presence of precipitation, the mean lowest clutter bin of the DPR-NS and DPR-MS are higher by 0.09 and 0.28 km, respectively. We noticed that in our stratiform events, the DPR-HS lowest clutter-free bottom is around 0.25 km higher than the convective event.

To review how the complex topography of the Andes affects the relationship between DPR scan angle and surface clutter height, we plotted the clutter depth of all DPR overpasses of the Mantaro Valley and the area surrounding it (within 12.45°–11.55°W, and 75.75°–74.85°S). Figure 9 shows how the depth of the DPR clutter region, defined as the difference between the height of the lowest clutter-free bin and real surface bin, is related to altitude and scan angle. The color of the dots in Fig. 9 indicates the depth of the clutter region. The aforementioned relationship between the scan angle and the clutter height of the DPR-NS is also evident in Fig. 9a.

4. Discussion

Above ML, the reflectivity of the DPR is up to 8 dBZ higher than that of the MIRA-35C (both measured and attenuation-corrected reflectivity). However, closer values (with less error) are observed between 4.5 and 5.5 km MSL (Fig. 4), which usually coincide with the DPR's lowest clutter-free bin, and as well are usually above the ML. In the corrected Z profiles of the DPR, a large part of the variability of the precipitation near the surface is lost due to the detected lowest clutter-free bin, consequently the variability of the R, D_m, and N_w profiles is also lost. Despite the DPR's lowest clutter-free bin occurring near the ML in these stratiform events, the correction performed by 2ADPR produced a DPR reflectivity profile that agrees rather well with the MIRA-35C below the ML, with an average bias of less than 3 dBZ near the surface. Except for E4 where MIRA-35C measures at least 10 dBZ less than DPR in the lowest clutter-free bin, this discrepancy is possibly caused by a potential non-precipitation-related calibration issue in MIRA-35C. Unfortunately, no data are available from Parsivel[2] to assess radar reflectivity. The DSD bias in stratiform events are affected by the height of lowest clutter-free bin often found near the ML where 2ADPR must employ assumptions about the complex fall velocity and dielectric properties of melting particles (Iguchi et al. 2018).

Our results on the mean lowest clutter-free bin is in agreement with the observations of Chavez et al. (2020), who found that the height of the lowest clutter-free bin in the Mantaro Valley ranged from 0.9 to 2 km MSL. In the southern Appalachians, the height of the ground clutter was observed between 1.3 and 3 km AGL (Arulraj and Barros 2019b). We observe that the height of the clutter is around 1.2 km AGL, but the average of the algorithm-detected lowest clutter-free bin is

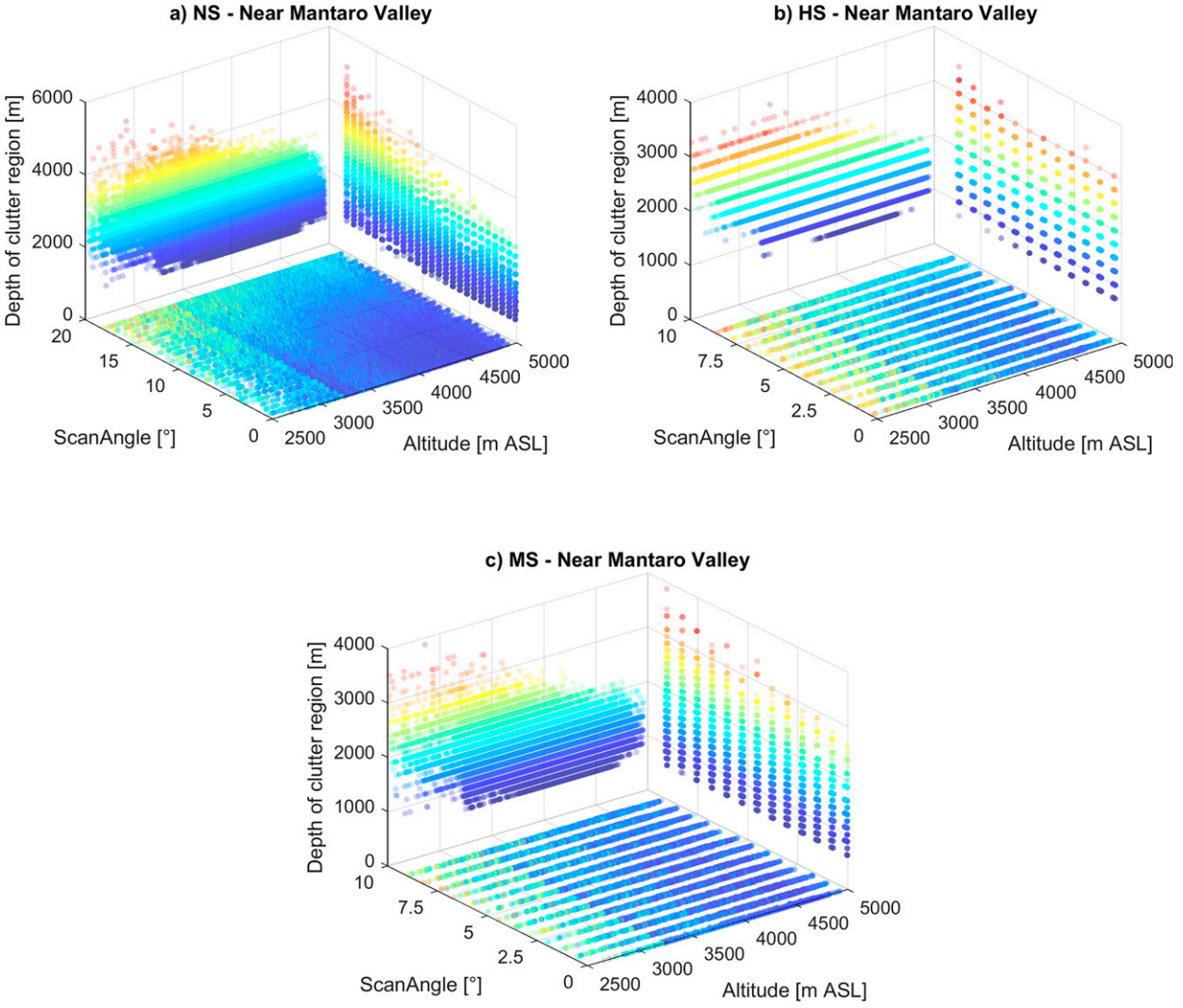

FIG. 9. (a) DPR-NS, (b) DPR-HS, and (c) DPR-MS depth of clutter region (z axis) in relation to altitude (x axis) and scan angle (y axis) over the Mantaro Valley and surrounding area (within 12.45°–11.55°W, and 75.75°–74.85°S). Note that the shading color indicates the depth of the clutter region (z axis).

1.62 ± 0.4 km AGL. Furthermore, the results presented in Fig. 6 indicate the nature of precipitation affects the 2ADPR-HS estimation of the clutter-free bottom and its close proximity to the ML strongly suggests the mixed phase is adversely impacting the algorithm-detected depth of the blind zone. However, this may be exacerbated by sidelobe effects from the wet terrain since stratiform would be more widespread than the convective.

The average DPR-NS ground clutter height is similar to that of DPR-HS, but the impact of its wider swath is evident in the amount of variability. However, the problem with the ground clutter is expected to be worse with data past 21 May 2018 because the new Ka-HS scans are now at more oblique angles, resulting in a greater height of the ground clutter.

The single polarization of MIRA-35C allows us to identify the ML, which is useful to compare its height with that of the DPR clutter in this study. The linear depolarization ratio (LDR) is a measure of particle shape and orientation relative to the radar beam and is enhanced for wet and melting particles, and as such it is often used to identify boundaries of the ML (e.g., Russchenberg 1991; Li and Moisseev 2020). Hence, we use MIRA-35C measurements of LDR in this study to identify the ML. An analysis of MIRA-35C's measurements of the LDR during the period 2016–17 indicates the ML exhibits little variability in height throughout the year (Fig. 10). Furthermore, the frequency of occurrence of ML height, which we detected using LDR (Bauer-Pfunstein 2007), shown in Fig. 10b suggests that DPR's retrievals of stratiform rainfall below the ML are rarely obtained over the complex terrain of our study area. As a result, we expect DPR's precipitation estimates across our study area to be consistently low in stratiform precipitation. This is important because stratiform precipitation, although it occurs with about 40% more frequently

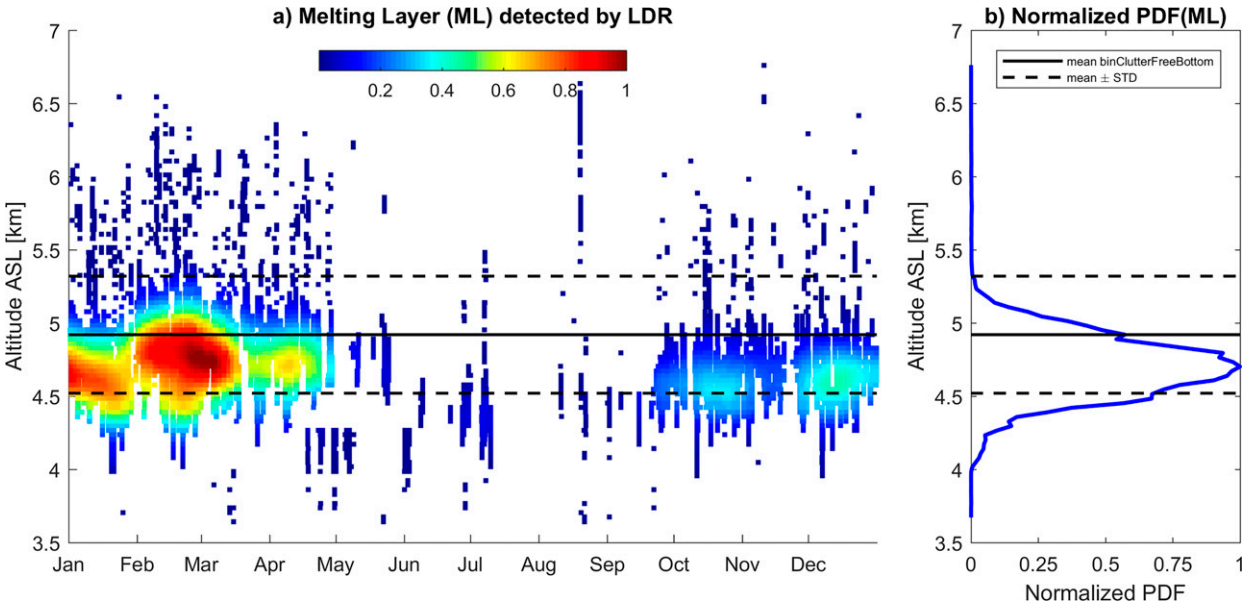

FIG. 10. (a) Normalized frequency of occurrence of ML height vs months, detected by MIRA-35C's LDR in the period of 2016–17. The black solid and dashed lines are mean $\mu \pm$ standard deviation σ of binClutterFreeBottom from Fig. 6a. (b) The ML height PDF normalized such that maximum occurrence is unity. The black solid and dashed lines are the same as in (a).

than convective precipitation (Villalobos et al. 2019; Poveda et al. 2020), it accounts for 37% of the annual precipitation at Huancayo Observatory.

There seems to be an inverse relationship between the altitude and the depth of the clutter (i.e., the lower the altitude, the greater the depth of the clutter), and this relationship is intensified at higher scan angles. In DPR-NS, at altitudes close to 2500 m MSL and scanning angles close to 20° it can be observed that the depth of the clutter region can extend up to 5 km (Fig. 9a), the highest values recorded in this study.

Given the relationship of the scan angle with the ground clutter, it is possible to find a statistical relationship that allows a better estimate of the average depth of the clutter region in the area, similar to that proposed by Kubota et al. (2016).

5. Summary and conclusions

In this work we used a Ka-band profiler (MIRA-35C) located at the Huancayo Observatory to evaluate simultaneous observations with GPM-DPR over the central Andes of Peru. The motivation for this study is to gain a better understanding of spaceborne precipitation estimation across complex topography. Of the 157 DPR overpasses of this Andean region between 2014 to early 2018, precipitation was observed in only six of overpasses coincident with the MIRA-35C observations. To address the differences in sampling volumes, we used an approach based on Taylor's hypothesis of frozen turbulence assuming a laminar atmosphere that determines the amount of temporal averaging to apply to the MIRA-35C observations. For the two stratiform cases, we find no significant differences in averaging times, whereas a longer averaging time (i.e., $\pm\Delta t$) tends to reduce the DPR bias in convective precipitation.

The DPR-based precipitation estimates over this region are greatly impacted by ground clutter. The 2ADPR algorithm places the lowest clutter-free bin well above the ground and often within the melting layer (>1.2 km AGL), especially for the HS scans. The presence of precipitation suggests a deeper 2ADPR blind zone, increasing the mean lowest clutter-free bin by 0.22 km at the Huancayo Observatory. Furthermore, the stratiform events have a deeper blind zone than the convective events. Consequently, this causes DPR to overestimate D_m (mean bias of 0.4 mm), which in turn produces an underestimate of N_w by nearly and order of magnitude (from -0.8 to -1.0 in logarithmic units of $\text{mm}^{-1}\ \text{m}^{-3}$). However, these biases tend to offset such that R estimated near the surface was within 1 mm h^{-1} of that retrieved by MIRA-35C. The results of this study suggest that DPR's near surface estimates of stratiform precipitation occurring within the central Andes is commonly obtained from its measurements within or just above the ML due to the blind zone, which is deeper in presence of precipitation. Therefore, long-term satellite-based radar estimates of precipitation will be underestimated in stratiform rainfall unless appropriate measures can be developed to mitigate these blind zone effects.

The impact of the DPR-HS scan angle is not evident in our study area. DPR-NS estimates, on the other hand, are severely affected by scan angle, and its effect on clutter region is evident. The DPR-MS has shown to have a better performance in estimating the clutter in our study area, whose depth on average is 0.32 km lower than the DPR-HS. It is important to note that an inverse relationship exists between the depth

of the clutter and the surface altitude in the Andes (i.e., DPR measurements in higher altitudes have a shallower depth of surface clutter). Future study is needed to better understand this finding.

It is very likely that DPR data after 21 May 2018, will have greater problems with ground clutter because of the change of the scan pattern in the DPR, where the new Ka-HS scans have more oblique angles that would result in a greater depth of the clutter region. One possible way to mitigate clutter effects in the area is to estimate the mean clutter height as a function of the scan angle. This statistical relationship could be used to rerun the estimates of the raw GPM-DPR Z with a local correction of the problem.

The results presented herein highlight some potential areas for improving satellite-based radar precipitation retrieval algorithms. In particular, they provide a more detailed depiction of the vertical variability of drop size distribution within the blind zone, which could possibly be accounted for using radar-observed melting layer characteristics (e.g., Gatlin et al. 2018), and demonstrate the effects of complex terrain on satellite-based precipitation estimates. Another approach to improving precipitation retrievals below DPR's lowest clutter-free bin over this region could use numerical weather prediction to depict the low-level orographic precipitation enhancement (e.g., Arulraj and Barros 2019a).

Acknowledgments. Thanks are given to Instituto Geofísco del Perú staff for their help with radar maintenance and data collection of MIRA-35C and BLTR. This study comes under the project "MAGNET-IGP: Strengthening the research line in physics and microphysics of the atmosphere (Agreement 010-2017-FONDECYT)." This work was done using computational resources of the HPC-Linux Cluster from the Laboratorio de Dinmica de Fluidos Geofísicos Computacionales at Instituto Geofísico del Perú (Grants 101-2014- FONDECYT, SPIRALES2012 IRD-IGP, Manglares IGP-IDRC, PP068 program). Authors Gatlin and Petersen thank NASA's GPM project for continued Cal/Val support. We gratefully thank anonymous reviewer 1 for the very careful reading of this paper and constructive comments that helped improve its quality.

Data availability statement. The GPM 2ADPR, version 06, product data used during this study are openly available from the NASA's Precipitation Processing System (https://doi.org/10.5067/GPM/DPR/GPM/2A/06). The authors were unable to find a valid MIRA-35C data repository for the data used in this study. These data are available from fsilva@igp.gob.pe or jvaldivia@igp.gob.pe at Instituto Geofísico del Perú.

REFERENCES

Arulraj, M., and A. P. Barros, 2019a: Towards a physically-based orographic precipitation retrieval correction algorithm for GPM-DPR using numerical weather prediction model simulations and ground-based observations. *2019 Fall Meeting*, San Francisco, CA, Amer. Geophys. Union, Abstract H13P-1980.

——, and ——, 2019b: Improving quantitative precipitation estimates in mountainous regions by modelling low-level seeder-feeder interactions constrained by Global Precipitation Measurement Dual-frequency Precipitation Radar measurements. *Remote Sens. Environ.*, **231**, 111213, https://doi.org/10.1016/j.rse.2019.111213.

Atlas, D., R. C. Srivastava, and R. S. Sekhon, 1973: Doppler radar characteristics of precipitation at vertical incidence. *Rev. Geophys.*, **11**, 1–35, https://doi.org/10.1029/RG011i001p00001.

Barrett, B. S., R. Garreaud, and M. Falvey, 2009: Effect of the Andes cordillera on precipitation from a midlatitude cold front. *Mon. Wea. Rev.*, **137**, 3092–3109, https://doi.org/10.1175/2009MWR2881.1.

Bauer-Pfunstein, M. R., 2007: Target separation and classification using cloud radar doppler-spectra. *33rd Conf. on Radar Meteorology*, Cairns, Australia, Amer. Meteor. Soc., 11.B2, https://ams.confex.com/ams/pdfpapers/123456.pdf.

Cao, Q., Y. Hong, J. J. Gourley, Y. Qi, J. Zhang, Y. Wen, and P.-E. Kirstetter, 2013: Statistical and physical analysis of the vertical structure of precipitation in the mountainous west region of the united states using 11+ years of spaceborne observations from TRMM precipitation radar. *J. Appl. Meteor. Climatol.*, **52**, 408–424, https://doi.org/10.1175/JAMC-D-12-095.1.

——, T. H. Painter, W. R. Currier, J. D. Lundquist, and D. P. Lettenmaier, 2018: Estimation of precipitation over the OLYMPEX domain during winter 2015/16. *J. Hydrometeor.*, **19**, 143–160, https://doi.org/10.1175/JHM-D-17-0076.1.

Cardona, O. D., and Coauthors, 2012: Determinants of risk: Exposure and vulnerability. *Managing the Risks of Extreme Events and Disasters to Advance Climate Change Adaptation*, C. B. Field et al., Eds., Cambridge University Press, 65–108, https://doi.org/10.1017/CBO9781139177245.005.

Chavez, S. P., Y. Silva, and A. P. Barros, 2020: High-elevation monsoon precipitation processes in the central Andes of Peru. *J. Geophys. Res. Atmos.*, **125**, e2020JD032947, https://doi.org/10.1029/2020JD032947.

Das, S., and A. Maitra, 2016: Vertical profile of rain: Ka band radar observations at tropical locations. *J. Hydrol.*, **534**, 31–41, https://doi.org/10.1016/j.jhydrol.2015.12.053.

Del Castillo-Velarde, C., S. Kumar, J. M. Valdivia-Prado, A. S. Moya-Álvarez, J. L. Flores-Rojas, E. Villalobos-Puma, D. Martínez-Castro, and Y. Silva-Vidal, 2021: Evaluation of GPM dual-frequency precipitation radar algorithms to estimate drop size distribution parameters, using ground-based measurement over the central Andes of Peru. *Earth Syst. Environ.*, **5**, 597–619, https://doi.org/10.1007/s41748-021-00242-5.

Derin, Y., and Coauthors, 2019: Evaluation of GPM-era Global Satellite Precipitation products over multiple complex terrain regions. *Remote Sens.*, **11**, 2936, https://doi.org/10.3390/rs11242936.

Flores-Rojas, J. L., and Coauthors, 2021a: Analysis of extreme meteorological events in the central Andes of Peru using a set of specialized instruments. *Atmosphere*, **12**, 408, https://doi.org/10.3390/atmos12030408.

——, and Coauthors, 2021b: On the dynamic mechanisms of intense rainfall events in the central Andes of Peru, Mantaro Valley. *Atmos. Res.*, **248**, 105188, https://doi.org/10.1016/j.atmosres.2020.105188.

Foote, G. B., and P. S. Du Toit, 1969: Terminal velocity of raindrops aloft. *J. Appl. Meteor.*, **8**, 249–253, https://doi.org/10.1175/1520-0450(1969)008<0249:TVORA>2.0.CO;2.

Furukawa, K., K. Yamamoto, T. Kubota, R. Oki, and T. Iguchi, 2018: Scan pattern change test operations of the dual-frequency precipitation radar on the Global Precipitation Measurement core spacecraft. *IGARSS 2018—2018 Int. Geoscience and Remote Sensing Symp.*, Valencia, Spain, IEEE, 8331–8334, https://doi.org/10.1109/IGARSS.2018.8518305.

Gatlin, P. N., W. A. Petersen, K. R. Knupp, and L. D. Carey, 2018: Observed response of the raindrop size distribution to changes in the melting layer. *Atmosphere*, **9**, 319, https://doi.org/10.3390/atmos9080319.

Germann, U., G. Galli, M. Boscacci, and M. Bolliger, 2006: Radar precipitation measurement in a mountainous region. *Quart. J. Roy. Meteor. Soc.*, **132**, 1669–1692, https://doi.org/10.1256/qj.05.190.

Gunn, R., and G. D. Kinzer, 1949: The terminal velocity of fall for water droplets in stagnant air. *J. Meteor.*, **6**, 243–248, https://doi.org/10.1175/1520-0469(1949)006%3C0243:TTVOFF%3E2.0.CO;2.

Hildebrand, P. H., and R. S. Sekhon, 1974: Objective determination of the noise level in Doppler spectra. *J. Appl. Meteor.*, **13**, 808–811, https://doi.org/10.1175/1520-0450(1974)013<0808:ODOTNL>2.0.CO;2.

Hou, A. Y., and Coauthors, 2014: The Global Precipitation Measurement mission. *Bull. Amer. Meteor. Soc.*, **95**, 701–722, https://doi.org/10.1175/BAMS-D-13-00164.1.

Houze, R. A., Jr., 2012: Orographic effects on precipitating clouds. *Rev. Geophys.*, **50**, RG1001, https://doi.org/10.1029/2011RG000365.

Iguchi, T., and R. Meneghini, 2017: GPM DPR Precipitation Profile L2A 1.5 hours 5 km V06. NASA Goddard Earth Sciences Data and Information Services Center, accessed March 2017, https://doi.org/10.5067/GPM/DPR/GPM/2A/06.

——, and Coauthors, 2018: GPM/DPR Level-2 algorithm theoretical basis document. NASA Goddard Space Flight Center Rep., 127 pp., https://pps.gsfc.nasa.gov/Documents/ATBD_DPR_201811_with_Appendix3b.pdf.

Joss, J., and R. Lee, 1995: The application of radar–gauge comparisons to operational precipitation profile corrections. *J. Appl. Meteor.*, **34**, 2612–2630, https://doi.org/10.1175/1520-0450(1995)034<2612:TAORCT>2.0.CO;2.

Junquas, C., K. Takahashi, T. Condom, J.-C. Espinoza, S. Chavez, J.-E. Sicart, and T. Lebel, 2018: Understanding the influence of orography on the precipitation diurnal cycle and the associated atmospheric processes in the central Andes. *Climate Dyn.*, **50**, 3995–4017, https://doi.org/10.1007/s00382-017-3858-8.

Kubota, T., T. Iguchi, M. Kojima, L. Liao, T. Masaki, H. Hanado, R. Meneghini, and R. Oki, 2016: A statistical method for reducing sidelobe clutter for the Ku-band precipitation radar on board the GPM *Core Observatory*. *J. Atmos. Oceanic Technol.*, **33**, 1413–1428, https://doi.org/10.1175/JTECH-D-15-0202.1.

Lee, G. W., A. W. Seed, and I. Zawadzki, 2007: Modeling the variability of drop size distributions in space and time. *J. Appl. Meteor. Climatol.*, **46**, 742–756, https://doi.org/10.1175/JAM2505.1.

Li, H., and D. Moisseev, 2020: Two layers of melting ice particles within a single radar bright band: Interpretation and implications. *Geophys. Res. Lett.*, **47**, e2020GL087499, https://doi.org/10.1029/2020GL087499.

Maahn, M., and P. Kollias, 2012: Improved Micro Rain Radar snow measurements using Doppler spectra post-processing. *Atmos. Meas. Tech.*, **5**, 2661–2673, https://doi.org/10.5194/amt-5-2661-2012.

Mantas, V. M., Z. Liu, C. Caro, and A. J. S. C. Pereira, 2015: Validation of TRMM multi-satellite precipitation analysis (TMPA) products in the Peruvian Andes. *Atmos. Res.*, **163**, 132–145, https://doi.org/10.1016/j.atmosres.2014.11.012.

Derin, Y., and Coauthors, 2016: Multiregional satellite precipitation products evaluation over complex terrain. *J. Hydrometeor.*, **17**, 1817–1836, https://doi.org/10.1175/JHM-D-15-0197.1.

Martínez-Castro, D., S. Kumar, J. L. Flores Rojas, A. Moya-Álvarez, J. M. Valdivia-Prado, E. Villalobos-Puma, C. D. Castillo-Velarde, and Y. Silva-Vidal, 2019: The impact of micro physics parameterization in the simulation of two convective rainfall events over the central Andes of Peru using WRF-ARW. *Atmosphere*, **10**, 442, https://doi.org/10.3390/atmos10080442.

Mourre, L., T. Condom, C. Junquas, T. Lebel, J. E. Sicart, R. Figueroa, and A. Cochachin, 2016: Spatio-temporal assessment of WRF, TRMM and in situ precipitation data in a tropical mountain environment (Cordillera Blanca, Peru). *Hydrol. Earth Syst. Sci.*, **20**, 125–141, https://doi.org/10.5194/hess-20-125-2016.

Moya-Álvarez, A. S., J. Gálvez, A. Holguín, R. Estevan, S. Kumar, E. Villalobos, D. Martínez-Castro, and Y. Silva, 2018a: Extreme rainfall forecast with the WRF-ARW Model in the central Andes of Peru. *Atmosphere*, **9**, 362, https://doi.org/10.3390/atmos9090362.

——, D. Martínez-Castro, J. L. Flores, and Y. Silva, 2018b: Sensitivity study on the influence of parameterization schemes in WRF-ARW Model on short- and medium-range precipitation forecasts in the central Andes of Peru. *Adv. Meteor.*, **2018**, 1381092, https://doi.org/10.1155/2018/1381092.

——, ——, S. Kumar, R. Estevan, and Y. Silva, 2019: Response of the WRF model to different resolutions in the rainfall forecast over the complex Peruvian orography. *Theor. Appl. Climatol.* **137**, 2993–3007, https://doi.org/10.1007/s00704-019-02782-3.

Peel, M. C., B. L. Finlayson, and T. A. McMahon, 2007: Updated world map of the Köppen-Geiger climate classification. *Hydrol. Earth Syst. Sci.*, **11**, 1633–1644, https://doi.org/10.5194/hess-11-1633-2007.

Peters, G., B. Fischer, and T. Andersson, 2002: Rain observations with a vertically looking Micro Rain Radar (MRR). *Boreal Environ. Res.*, **7**, 353–362.

——, ——, H. Münster, M. Clemens, and A. Wagner, 2005: Profiles of raindrop size distributions as retrieved by microrain radars. *J. Appl. Meteor.*, **44**, 1930–1949, https://doi.org/10.1175/JAM2316.1.

——, ——, and M. Clemens, 2010: Rain attenuation of radar echoes considering finite range resolution and using drop size distributions. *J. Atmos. Oceanic Technol.*, **27**, 829–842, https://doi.org/10.1175/2009JTECHA1342.1.

Poveda, G., J. C. Espinoza, M. D. Zuluaga, S. A. Solman, R. Garreaud, and P. J. van Oevelen, 2020: High impact weather events in the Andes. *Front. Earth Sci.*, **8**, 162, https://doi.org/10.3389/feart.2020.00162.

Ralph, F. M., 1995: Using radar-measured radial vertical velocities to distinguish precipitation scattering from clear-air scattering. *J. Atmos. Oceanic Technol.*, **12**, 257–267, https://doi.org/10.1175/1520-0426(1995)012%3C0257:URMRVV%3E2.0.CO;2.

Rao, T. N., D. N. Rao, and S. Raghavan, 1999: Tropical precipitating systems observed with Indian MST radar. *Radio Sci.*, **34**, 1125–1139, https://doi.org/10.1029/1999RS900054.

Roe, G. H., 2005: Orographic precipitation. *Annu. Rev. Earth Planet. Sci.*, **33**, 645–671, https://doi.org/10.1146/annurev.earth.33.092203.122541.

Russchenberg, H., 1991: Doppler-polarimetric radar measurements of the melting layer of precipitation. *1991 Seventh Int. Conf. on Antennas and Propagation*, York, United Kingdom, IEEE, 76–79.

Scheel, M. L. M., M. Rohrer, C. Huggel, D. Santos Villar, E. Silvestre, and G. J. Huffman, 2011: Evaluation of TRMM Multi-satellite Precipitation Analysis (TMPA) performance in the central Andes region and its dependency on spatial and temporal resolution. *Hydrol. Earth Syst. Sci.*, **15**, 2649–2663, https://doi.org/10.5194/hess-15-2649-2011.

Skofronick-Jackson, G., D. Kirschbaum, W. Petersen, G. Huffman, C. Kidd, E. Stocker, and R. Kakar, 2018: The Global Precipitation Measurement (GPM) mission's scientific achievements and societal contributions: Reviewing four years of advanced rain and snow observations. *Quart. J. Roy. Meteor. Soc.*, **144**, 27–48, https://doi.org/10.1002/qj.3313.

Speirs, P., M. Gabella, and A. Berne, 2017: A comparison between the GPM dual-frequency precipitation radar and ground-based radar precipitation rate estimates in the Swiss Alps and Plateau. *J. Hydrometeor.*, **18**, 1247–1269, https://doi.org/10.1175/JHM-D-16-0085.1.

Taylor, G. I., 1938: The spectrum of turbulence. *Proc. Roy. Soc.*, **164A**, 476–490, https://doi.org/10.1098/rspa.1938.0032.

Valdivia, J. M., K. Contreras, D. Martinez-Castro, E. Villalobos-Puma, L. F. Suarez-Salas, and Y. Silva, 2020a: Dataset on raindrop size distribution, raindrop fall velocity and precipitation data measured by disdrometers and rain gauges over Peruvian central Andes (12.0°S). *Data Brief*, **29**, 105215, https://doi.org/10.1016/j.dib.2020.105215.

——, D. E. Scipión, M. Milla, and Y. Silva, 2020b: Multi-instrument rainfall-rate estimation in the Peruvian central Andes. *J. Atmos. Oceanic Technol.*, **37**, 1811–1826, https://doi.org/10.1175/JTECH-D-19-0105.1.

Viale, M., and F. A. Norte, 2009: Strong cross-barrier flow under stable conditions producing intense winter orographic precipitation: A case study over the subtropical central Andes. *Wea. Forecasting*, **24**, 1009–1031, https://doi.org/10.1175/2009WAF2222168.1.

Villalobos, E. E., D. Martinez-castro, S. Kumar, Y. Silva, and O. Fashe, 2019: Estudio de tormentas convectivas sobre los Andes centrales del Perú usando los radares PR-TRMM (Study of convective storms in the Peruvian central Andes using the PR-TRMM radar). *Rev. Cubana Meteor.*, **25**, 59–75, http://opn.to/a/tG8c1.

Welle, T., and J. Birkmann, 2015: The world risk index—An approach to assess risk and vulnerability on a global scale. *J. Extreme Events*, **2**, 1550003, https://doi.org/10.1142/S2345737615500037.

Wen, Y., P. Kirstetter, Y. Hong, J. J. Gourley, Q. Cao, J. Zhang, Z. Flamig, and X. Xue, 2016: Evaluation of a method to enhance real-time, ground radar–based rainfall estimates using climatological profiles of reflectivity from space. *J. Hydrometeor.*, **17**, 761–775, https://doi.org/10.1175/JHM-D-15-0062.1.

Zawadzki, I. I., 1973: Statistical properties of precipitation patterns. *J. Appl. Meteor.*, **12**, 459–472, https://doi.org/10.1175/1520-0450(1973)012%3C0459:SPOPP%3E2.0.CO;2.